atmosphere

MDPI

Article

Spatiotemporal Characteristics of Carbon Fluxes and Their Environmental Drivers in a Plateau Urban Wetlands Ecosystem Based on Eddy Covariance Observations

Jiankang Ling [1,2], Xufeng Mao [1,2,*], Xiaoyan Wei [3], Xiuhua Song [4], Lele Zhang [1,2], Hongyan Yu [5], Yongxiao Yang [1,2], Jintao Zhang [1,2] and Shunbang Xie [4]

[1] Key Laboratory of Tibetan Plateau Land Surface Processes and Ecological Conservation, Ministry of Education, Qinghai Normal University, Xining 810008, China; jkl_sn@outlook.com (J.L.)
[2] Qinghai Province Key Laboratory of Physical Geography and Environmental Process, College of Geographical Science, Qinghai Normal University; Xining 810008, China
[3] School of Economics and Management, Qinghai Normal University, Xining 810008, China
[4] Management and Service Center for Huangshui National Wetland Park, Xining 810016, China
[5] Management and Service Center of Qilian Mountain National Park, Xining 810008, China
* Correspondence: maoxufeng@yeah.net

Abstract

Urban wetlands on the Qinghai–Tibetan Plateau are increasingly recognized as potentially important components of city-scale carbon budgets; however, their CO_2 flux dynamics and associated environmental drivers remain insufficiently quantified, particularly under high-altitude urban conditions. In this study, we addressed this knowledge gap by conducting continuous eddy covariance observations at Haihu Wetland Park in Xining City, China. Carbon fluxes were monitored throughout 2023 using the Huangshui Park Station flux tower. We quantified the temporal dynamics of gross primary productivity (GPP), ecosystem respiration (Re), and net ecosystem exchange (NEE), and systematically assessed their responses to key environmental drivers across multiple temporal scales. GPP and Re exhibited unimodal seasonal patterns, with substantially higher values during the growing season. NEE showed pronounced diel cycling, with nighttime CO_2 release and daytime uptake, and shifted seasonally between net source and net sink states. At the daily scale (n = 365), Pearson correlations showed that air temperature (T_a), 5 cm soil temperature (T_{s5}) and volumetric soil water content (SWC) exhibited the strongest associations with the flux components, whereas photosynthetic photon flux density (PPFD) showed moderate associations and precipitation was weak. At the monthly scale (n = 12), Mantel tests further highlighted a dominant thermal control on GPP and Re (T_a and T_{s5}), whereas precipitation showed additional associations with Re and NEE. Overall, the ecosystem acted as a net CO_2 sink in 2023 (annual NEE = -292.25 g C m^{-2} yr^{-1} under our sign convention), with uptake concentrated in the first eight months of the year. Under the combined effects of multiple environmental factors, plateau urban wetlands functioned as a strong carbon sink, and the results of this study provide a data basis for improving the accuracy of carbon budget estimates for this type of ecosystem.

Keywords: urban wetlands carbon budget; eddy covariance; carbon flux components; hydrothermal controls

Academic Editor: Enrico Ferrero

Received: 4 January 2026
Revised: 10 February 2026
Accepted: 19 February 2026
Published: 20 February 2026

1. Introduction

The accelerated pace of global urbanization has driven widespread land-cover conversion worldwide, often replacing high-carbon-sequestration ecosystems (e.g., wetlands and grasslands) with impervious or intensively managed surfaces, thereby reshaping urban carbon source–sink dynamics [1–5]. In response to these challenges, urban wetland ecological engineering, which integrates habitat restoration with landscape and hydrological functions, has been increasingly implemented as a nature-based solution to enhance urban carbon uptake and climate resilience. Urban wetlands are wetlands embedded within urban landscapes and influenced by urban hydrology, land use, and human activities [6,7]. As integral components of urban ecosystems, they provide essential ecosystem services, including carbon sequestration and the regulation of regional carbon cycling [8,9]. Accordingly, continuous monitoring of ecosystem CO_2 exchange and quantification of its relationships with key environmental drivers have become research priorities for improving the assessment and management of urban carbon budgets [10].

A variety of methods have been developed to monitor ecosystem carbon exchange [11]. Early studies primarily relied on manual in situ measurements using static chambers coupled with gas chromatography, but such measurements are discontinuous and cannot capture integrated flux dynamics at ecosystem scales. With advances in micrometeorological observations, the eddy covariance (EC) technique has become one of the dominant approaches for monitoring CO_2 exchange [12–15]. The EC technique determines CO_2 fluxes by calculating the covariance between CO_2 concentration fluctuations and vertical wind velocity over a given unit area and time. Owing to its advantages of continuous in situ observations, minimal disturbance to natural environments, large spatial representativeness, and high temporal resolution, EC has been widely applied and has played a critical role in carbon flux studies of typical terrestrial ecosystems, including forests, grasslands, and croplands [16]. Consequently, carbon flux research in these terrestrial ecosystems has become a major focus [17–20].

In addition, the eddy covariance (EC) technique has been widely applied to various wetland ecosystems (including coastal salt marshes and restored wetlands) as well as urban ecosystems to quantify CO_2 and energy fluxes and to examine their responses to changing environmental conditions [21]. Syntheses based on multi-site EC observations have further explored the spatiotemporal variability of CO_2 fluxes and their environmental controls across different wetland types (e.g., coastal wetlands) [22]. In China's high-altitude natural wetlands (e.g., alpine and tundra wetlands), long-term EC observations have revealed clear relationships between net ecosystem exchange (NEE) and key environmental drivers, including photosynthetically active radiation and soil temperature, offering important mechanistic insights into carbon cycling processes in high-altitude ecosystems [23]. These studies demonstrate the effectiveness and broad applicability of EC in monitoring carbon dynamics in complex ecosystems [24,25]. Moreover, urban greenhouse gas flux networks based on EC, such as INFLUX, have highlighted the potential of this framework for coordinated, multi-site monitoring of urban carbon sources and sinks, providing a global perspective and methodological reference for urban carbon cycle research [26].

However, long-term and continuous eddy covariance (EC) observations of plateau urban wetland ecosystems remain relatively scarce, particularly for urban wetlands on the Qinghai–Tibetan Plateau, which are highly sensitive to climate change and anthropogenic influences. The Qinghai–Tibetan Plateau, with an average elevation exceeding 4000 m, is commonly referred to as the "Third Pole of the World." Its unique geographical setting gives rise to distinct climatic conditions, under which organic carbon decomposition proceeds slowly, allowing large amounts of organic carbon to be preserved in deep soil layers over long timescales. As a result, the region represents the world's highest-altitude

carbon reservoir [27]. In addition, the Qinghai–Tibetan Plateau is rich in wetland resources and constitutes one of the most important wetland distribution regions in China [28]. However, climate warming has already altered wetland distribution patterns and ecosystem functioning across the plateau [29–32]. Therefore, under the global change context that necessitates a reassessment of future carbon storage potential [33], an in-depth investigation of carbon flux dynamics in urban wetlands on the Qinghai–Tibetan Plateau is of great significance for understanding regional wetland carbon budgets, carbon cycling, and carbon mitigation, and also provides a reference for carbon balance assessments of similar high-altitude urban ecosystems worldwide. This study investigates the spatiotemporal dynamics of ecosystem carbon fluxes in a plateau urban wetland using eddy covariance observations from Haihu Wetland Park, Xining. We analyze the responses of carbon flux components to key environmental drivers and assess the carbon source–sink status of the ecosystem, providing a basis for carbon budget evaluation in urban wetlands on the Qinghai–Tibetan Plateau.

2. Materials and Methods

2.1. Overview of the Study Area

This study was conducted in Haihu Wetland Park, Xining, on the northeastern Qinghai–Tibetan Plateau (Figure 1). The ecosystem eddy covariance observation and research station operated by the Qinghai Provincial Forestry and Grassland Administration is located within the park (Huangshui Park Station; 36°39′13.21″ N, 101°41′13.62″ E).

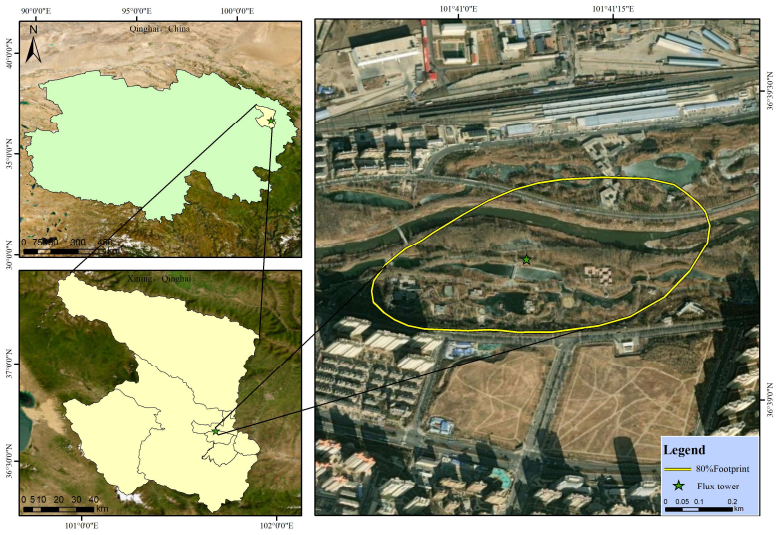

Figure 1. Geographic location of the eddy covariance (EC) flux tower at Haihu Wetland Park, Xining City, northeastern Qinghai–Tibetan Plateau, China (36°39′13.21″ N, 101°41′13.62″ E).

Haihu Wetland Park in Xining is located in the Hehuang Valley on the northeastern Qinghai–Tibetan Plateau and represents a typical plateau urban wetland ecosystem. The region is characterized by a plateau semi-arid climate, with relatively low mean annual air temperatures, pronounced diurnal temperature variations, and generally low precipitation that is unevenly distributed and mainly concentrated during the warm season. Strong solar radiation, low-temperature conditions, and distinct seasonal hydrothermal regimes jointly shape the unique ecological environment of the region. These climatic characteristics tend to slow organic matter decomposition and play an important role in regulating carbon accumulation and carbon exchange processes in wetland ecosystems. [34]. The eddy covariance flux tower is located in the central area of the park. The underlying surface within the flux source area is heterogeneous, consisting mainly of woodland, grassland,

and wetland patches. The vegetation is dominated by trees, with *Populus cathayana*, *Salix babylonica*, and *Pinus tabuliformis* as the major dominant species.

The underlying surface within the flux footprint area is heterogeneous, consisting mainly of woodland, grassland, and wetland patches. To quantify the flux source area, we applied the Flux Footprint Prediction (FFP) model [35–37] to estimate cumulative footprints and identify the 80% flux contribution zone, which exhibited a radial extent of 203–458 m with directional elongation in the northeast (40–90°) and southwest (200–260°) sectors. This defined the study area as the 80% flux-contributing footprint centered on the flux tower, ensuring that the EC observations were spatially representative of the land-cover variability in the park and minimizing uncertainty in the flux measurements.

2.2. Methodology

EC technique was used to quantify ecosystem–atmosphere CO_2 exchange and concurrent meteorological and soil conditions. The EC system consisted of a three-dimensional sonic anemometer (WindMaster Pro, Gill Instruments Ltd., Lymington, UK) and an open-path infrared gas analyzer (LI-7500DS, LI-COR Biosciences, Lincoln, NE, USA), sampling at 10 Hz. Auxiliary sensors included a PPFD sensor (LI-190R, LI-COR Biosciences, Lincoln, NE, USA), net radiometer (CNR4, Kipp & Zonen B.V., Delft, The Netherlands), soil heat flux plate (HFP01, Hukseflux Thermal Sensors B.V., Delft, The Netherlands), soil moisture probe (Hydro Probe, Campbell Scientific Inc., Logan, UT, USA; installed at 5 cm depth), air temperature and relative humidity sensor (HMP155A, Vaisala Oyj, Vantaa, Finland), and tipping-bucket rain gauge (TR-525, Texas Electronics Inc., Dallas, TX, USA) [38,39]. All variables were averaged over 30 min intervals (local time).

High-frequency raw data from 1 January to 31 December 2023 were processed in EddyPro (v7.0.9) to compute 30 min turbulent fluxes. Standard corrections were applied, including planar-fit coordinate rotation, time-lag compensation, frequency-response correction, and Webb–Pearman–Leuning (WPL) density correction [40,41]. Data gaps and outliers caused by instrument malfunction or abnormal meteorological conditions were identified and removed following objective criteria, and remaining gaps were subsequently filled to generate continuous time series [42]. Flux quality was screened using EddyPro diagnostic flags and quality flags (Foken classes) [43,44]. Post-processing and aggregation were conducted in Tovi (v2.8.1) for quality-control screening, visual inspection, and gap filling. Fluxes were removed when: (i) instrument diagnostic flags indicated malfunction; (ii) values equaled the missing-value flag (e.g., −9999); or (iii) flux quality fell below the accepted level (i.e., records flagged as quality class 2). Visual inspection was used only as a secondary check to confirm periods affected by instrument issues or abnormal meteorological events. A friction velocity (u*) threshold was determined from grouped nighttime data using the empirical quantile approach [45,46]. Nighttime was defined as PPFD < 10 μmol m^{-2} s^{-1}. Thresholds were estimated separately by season (defined following the meteorological convention: winter (DJF, December–February), spring (MAM, March–May), summer (JJA, June–August), and autumn (SON, September–November)) and the final site-specific u* threshold was set to 0.197 m s^{-1}. Flux records with u* below this threshold were excluded and subsequently gap-filled using the methods described in Section 2.3.

2.3. Data Handling

Data gaps in 30 min NEE were filled using commonly applied empirical response functions, with separate schemes for nighttime and daytime periods. For nighttime (PPFD < 10 μmol m^{-2} s^{-1}) under sufficient turbulence (u* $\geq$ 0.197 m s^{-1}), we fitted an ex-

ponential temperature–respiration relationship separately for the growing and non-growing seasons [47]:

$$NEE_{night} = a \times \exp(b \times T_a) \quad (1)$$

Parameters a and b, which are fitted based on quality-controlled data, were determined using seasonal thresholds defined according to local meteorological conventions, with T_a representing air temperature (°C). At night, photosynthesis is negligible and nighttime NEE is assumed to approximate Re. The fitted relationship was therefore used to predict missing nighttime NEE and to provide respiration estimates for flux partitioning.

For daytime periods during the growing season, missing NEE values were filled using a rectangular hyperbolic light response (Michaelis–Menten) function [48], with seasonal variation taken into account by fitting parameters monthly using quality-controlled daytime data:

$$NEE_{day} = -\left(\frac{\alpha \times PPFD \times P_{max}}{\alpha \times PPFD + P_{max}}\right) + R_d \quad (2)$$

where α is the apparent quantum yield, PPFD is photosynthetic photon flux density (μmol m^{-2} s^{-1}), P_{max} is the maximum photosynthetic capacity (μmol m^{-2} s^{-1}), and R_d is daytime respiration (μmol m^{-2} s^{-1}). Parameters were fitted on a monthly basis using quality-controlled daytime data, and the fitted function was used to predict NEE for time steps with missing daytime observations.

The gap-filling criteria, including the u* threshold of 0.197 m s^{-1}, were selected based on the method established by Foken et al. (2004) and validated with data from prior studies in similar ecosystems [45,49]. This threshold value was chosen to exclude data points with insufficient turbulence, as such conditions may lead to inaccurate flux measurements. These parameters were explicitly validated through visual inspection of the quality flags and flux diagnostic tools in EddyPro (v7.0.9), ensuring the results were representative and reliable. Additionally, a more stringent gap-filling method was applied in periods of high-frequency noise, ensuring that data consistency was maintained.

We adopted the standard sign convention in which NEE < 0 μmol m^{-2} s^{-1} indicates net CO_2 uptake (carbon sink) and NEE > 0 μmol m^{-2} s^{-1} indicates net CO_2 release (carbon source). Under nighttime conditions (PPFD < 10 μmol m^{-2} s^{-1}) and sufficient turbulence (u* $\geq$ 0.197 m s^{-1}), photosynthesis is negligible (GPP $\approx$ 0) and thus nighttime NEE can be approximated as Re. We fitted a temperature–respiration response function to quality-screened nighttime data using air temperature (T_a), with parameters estimated separately for each season. Ecosystem respiration for all time steps (including daytime) was then estimated by predicting Re from the fitted response function using the corresponding temperature at each 30 min time step [50]. Finally, GPP was obtained by flux partitioning based on:

$$NEE = Re - GPP \quad (3)$$

Rearranging Equation (3) yields:

$$GPP = Re - NEE \quad (4)$$

where NEE, Re, and GPP are all expressed in units of μmol m^{-2} s^{-1}.

During energy transfer processes within ecosystems, net radiation (Rn) was defined as positive for downward (toward the surface) radiative fluxes and negative for upward fluxes. The energy balance equation for eddy covariance flux measurements can be expressed as follows [39]:

$$R_n - G - S - Q = H + LE \quad (5)$$

In Equation (5), Rn is net radiation, G is soil heat flux, S denotes heat stored within the canopy, Q summarizes other minor storage terms, H is sensible heat flux, and LE is latent heat flux. In practical observations, the magnitudes of S and Q are relatively small and were therefore neglected. Under this assumption, the energy balance equation can be simplified as follows:

$$R_n - G = H + LE \quad (6)$$

In Equation (6), $R_n - G$ represents the available energy, while H + LE is referred to as turbulent energy. When the available energy equals the turbulent energy, the energy balance is considered closed; otherwise, a lack of closure is indicated. After quality control and data processing, linear regression of (H + LE) against ($R_n - G$) yielded a slope of 0.89, indicating a satisfactory level of energy balance closure in this study.

2.4. Statistical Methods

Carbon flux data were processed and analyzed using Microsoft Excel, EddyPro (v7.0.9), Tovi (v2.8.1), and Origin (2025b). Statistical analyses, including Pearson correlation analysis and Mantel tests, were performed using Chiplot Online (https://www.chiplot.com (accessed on 8 February 2026)), a web-based tool for statistical analysis. Pearson correlation analysis was performed at the daily scale using daily means (n = 365 after gap filling) to quantify linear associations between carbon flux components (GPP, Re, and NEE) and environmental variables. Mantel tests were conducted at the monthly scale (n = 12) using monthly aggregated data to reduce high-frequency noise and emphasize seasonal covariation patterns between fluxes and environmental conditions. Euclidean distance matrices were constructed for both sets, and the Mantel test was performed using Euclidean distances for both matrices. Significance was assessed using 999 permutations, and Mantel p-values are reported in the text and visualized using color coding.

3. Results

3.1. Temporal Variability of Gross Primary Productivity (GPP)

3.1.1. Diurnal Variation of GPP

GPP exhibited a pronounced diurnal cycle, peaking around midday and approaching zero at night when photosynthesis is negligible due to the absence of light. The monthly mean diurnal cycles of GPP were derived from the 2023 half-hourly estimates by averaging GPP at the same time of day within each month (Figure 2). GPP showed a pronounced diurnal cycle, with an inverted V-shaped curve, peaking around midday and approaching zero at night, when photosynthesis is negligible due to the absence of light. The annual maximum of the monthly mean diurnal peak occurred in September (21.86 μmol m^{-2} s^{-1}). To further characterize seasonal differences, we estimated the mean daily photosynthetically active duration as the period when GPP > 0 μmol m^{-2} s^{-1}. The growing season showed a longer duration than the non-growing season (11.8 h vs. 9.0 h on average), with the longest durations in June–July (13 h) and the shortest in January (7 h). Duration alone does not quantify photosynthetic strength or cumulative carbon uptake; nevertheless, it provides complementary evidence for seasonal variation in GPP. Notably, a longer active duration did not necessarily coincide with a higher diurnal peak. Although the photosynthetically active duration in May was longer than in October, the diurnal peak GPP was lower, which aligns with the relatively less favorable light and temperature conditions in May compared to October.

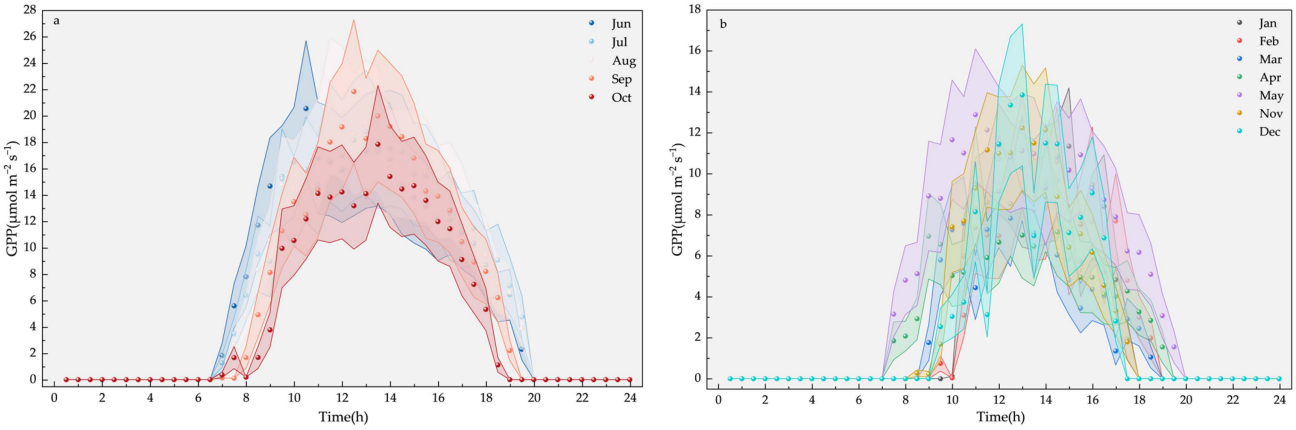

Figure 2. Monthly mean diurnal cycles of gross primary productivity (GPP) during the growing season (**a**) and non-growing season (**b**) at Haihu Wetland Park, Xining, northeastern Qinghai–Tibetan Plateau. Monthly mean values (symbols) were derived from half-hourly observations by averaging GPP at the same time of day within each month. Shaded areas represent ±1 standard deviation (SD), reflecting day-to-day variability within each month.

3.1.2. Annual Dynamics of GPP

GPP followed a distinct annual cycle, rising from late winter into spring, reaching a midsummer maximum and declining towards winter (Figure 3). The values remained consistently low during approximately DOY 1–90, increased through the main growing period (approximately DOY 90–240), and then decreased during autumn and early winter (approximately DOY 240–360), returning to levels similar to those observed at the beginning of the year. This temporal evolution agrees with the monthly patterns shown in Figure 2. The daily mean GPP peaked at 9.25 μmol m^{-2} s^{-1} (Figure 3), corresponding to the period of highest vegetation activity. To capture the dominant intra-annual periodicity, we fitted a sinusoidal function to the daily mean GPP series derived from quality-screened 30 min observations. Where x represents the day of the year (DOY; 1–365), the fitted model was: $GPP = 4.62 - 2.45 \sin(2\pi x/365 + 0.98)$. The model explained 71% of the variance ($R^2 = 0.71$), indicating that a single annual harmonic captures most of the seasonal signal in GPP at this site.

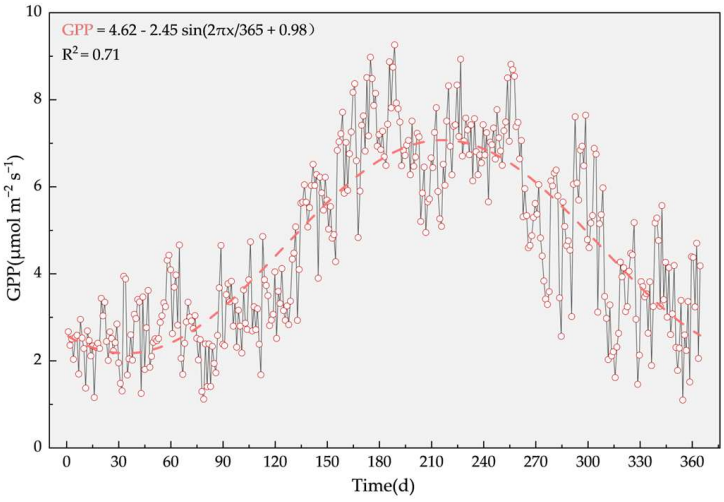

Figure 3. Annual variation in gross primary productivity (GPP) at Haihu Wetland Park, Xining, northeastern Qinghai–Tibetan Plateau. Open circles represent observed daily mean GPP values. The solid red line represents the fitted sinusoidal model ($GPP = 4.62 - 2.45 \sin(2\pi x/365 + 0.98)$), and the dashed line denotes the modeled GPP. The model explains 71% of the variance ($R^2 = 0.71$).

3.2. Temporal Variability of Ecosystem Respiration (Re)

3.2.1. Diurnal Variation of Re

Re showed clear diurnal variability, with greater short-term variability at night in the growing season compared to the daytime. In the growing season (Figure 4a), after sunrise, Re increased steadily, reached a clear maximum at approximately 16:00 local time, and then decreased toward evening. In the non-growing season (Figure 4b), Re was lower in magnitude throughout the day and varied more among months, yet the diel signal remained evident: Re increased after sunrise and attained its daily maximum near 20:00, several hours later than in the growing season. The highest monthly mean diurnal peak of Re in the growing season occurred in October (8.0 μmol m^{-2} s^{-1}), whereas the peak Re during the non-growing season occurred in November (4.2 μmol m^{-2} s^{-1}). Seasonal differences were also apparent in the magnitude of Re, which followed the order: mid-to-late growing season (July–October) > early growing season (June) > transitional months (May and November) > deep winter (January, February, and December).

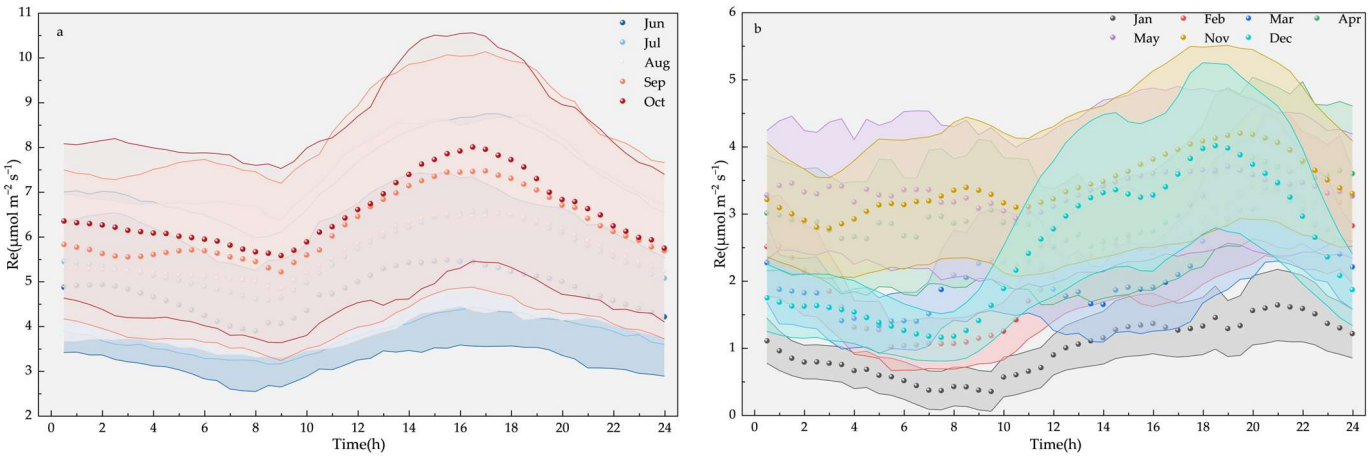

Figure 4. Monthly mean diurnal cycles of ecosystem respiration (Re) during the growing season (**a**) and non-growing season (**b**) at Haihu Wetland Park, Xining, northeastern Qinghai–Tibetan Plateau. Monthly mean values (symbols) were derived from half-hourly observations by averaging Re at the same time of day within each month. Shaded areas represent ±1 standard deviation (SD), reflecting day-to-day variability within each month.

3.2.2. Annual Dynamics of Re

Re showed a clear seasonal cycle, rising from low values early in the year to an annual maximum around DOY 300 and then dropping sharply toward winter (Figure 5). Re increased overall during the first approximately 300 days and peaked near DOY 300 at about 9.93 μmol m^{-2} s^{-1}. After the peak, Re declined rapidly and returned to levels comparable to those at the start of the year. This pattern aligns with the expected contrast between the growing and non-growing seasons. From spring into summer, Re generally increased alongside rising air temperature and radiation. From spring to summer, Re generally increased with rising air temperature and radiation, and elevated Re persisted into autumn. As late autumn approached, Re reached its peak, and then declined to its annual minimum following the onset of winter. To describe the temporal variability in Re, we fitted a sinusoidal function to the daily mean Re time series derived from the quality-controlled 30 min data. With x denoting day of year (DOY; 1–365), the fitted equation was: $Re = 3.8 - 2.27 \sin(2\pi x/365 + 0.72)$. The model explained a substantial portion of the intra-annual variability ($R^2 = 0.62$), indicating that a single seasonal harmonic captures the dominant annual pattern of Re at this site.

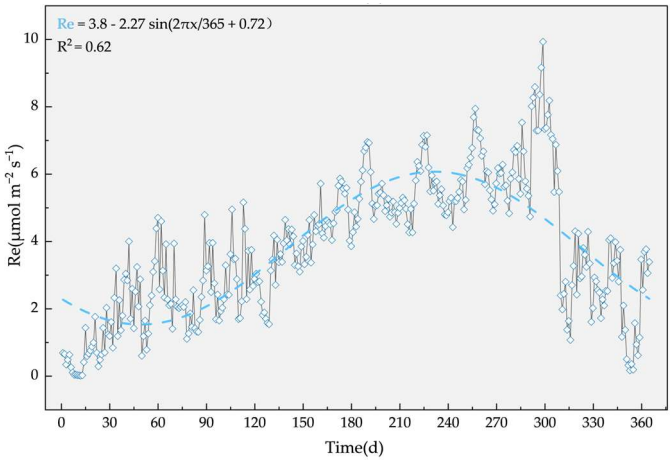

Figure 5. Annual variation in ecosystem respiration (Re) at Haihu Wetland Park, Xining, northeastern Qinghai–Tibetan Plateau. Open circles represent observed daily mean Re values. The solid blue line represents the fitted sinusoidal model ($Re = 3.80 - 2.27 \sin(2\pi x/365 + 0.72)$), and the dashed line denotes the modeled Re. The model explains 62% of the variance ($R^2 = 0.62$).

3.3. Temporal Variability of Net Ecosystem Exchange (NEE)

3.3.1. Diurnal Variation of NEE

NEE exhibited a pronounced diurnal pattern, with a midday trough indicating net CO_2 uptake, which then shifted to net CO_2 release in the early evening. In the non-growing season, a similar diurnal pattern was observed, but with a shorter daytime uptake window. NEE typically transitioned from positive to negative values between 08:00 and 10:00, with the daily minimum occurring around midday (10:00–13:00). In the late afternoon (17:00–18:30), NEE returned to positive values, marking a shift to net CO_2 release. Figure 6 illustrates the monthly mean diurnal pattern of NEE in 2023. The pattern was U-shaped in most months, with NEE reaching its daily minimum (most negative values) from late morning to early afternoon and progressively increasing in the evening (17:30–18:30), indicating a shift to net CO_2 release. In the non-growing season, the daytime uptake period was shorter, and the daily minimum occurred around midday (11:00–13:00), but the overall diurnal cycle remained similar to the growing season.

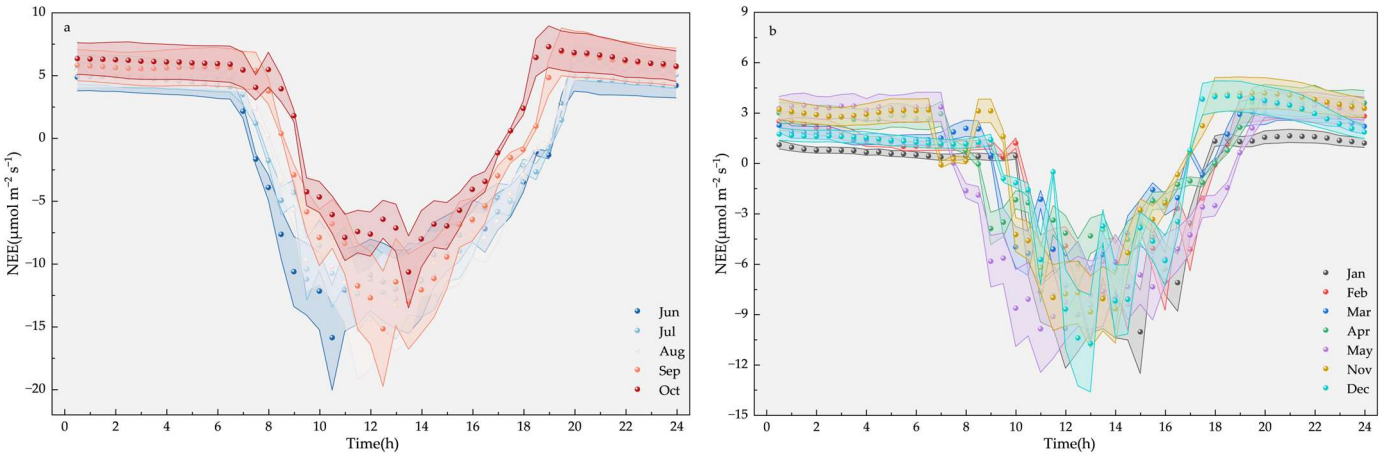

Figure 6. Monthly mean diurnal cycles of net ecosystem exchange (NEE) during the growing season (**a**) and non-growing season (**b**) at Haihu Wetland Park, Xining, northeastern Qinghai–Tibetan Plateau. Monthly mean values (symbols) were derived from half-hourly observations by averaging NEE at the same time of day within each month. Shaded areas represent ±1 standard deviation (SD), reflecting day-to-day variability within each month. Negative NEE values indicate net CO_2 uptake, whereas positive values indicate net CO_2 release.

3.3.2. Annual Dynamics of NEE

NEE followed a bimodal annual pattern, with transitions between net CO_2 sink and source (Figure 7). During DOY 1–90, NEE trended upward and became positive, indicating net CO_2 release in late winter to early spring when GPP remained low. From DOY 90 to 180, NEE crossed into negative values and declined further, reaching its annual minimum (strongest uptake) between DOY 150 and 180. Between DOY 180 and 270, NEE became less negative, indicating a weakened (but persistent) sink during summer. From DOY 270 to 360, NEE increased sharply, turned positive around DOY 300, and reached its annual maximum, indicating peak net carbon release. In autumn, Re increased while GPP decreased, leading to a temporary shift of the ecosystem to net carbon release. This increase in Re is consistent with the Re maximum observed in October.

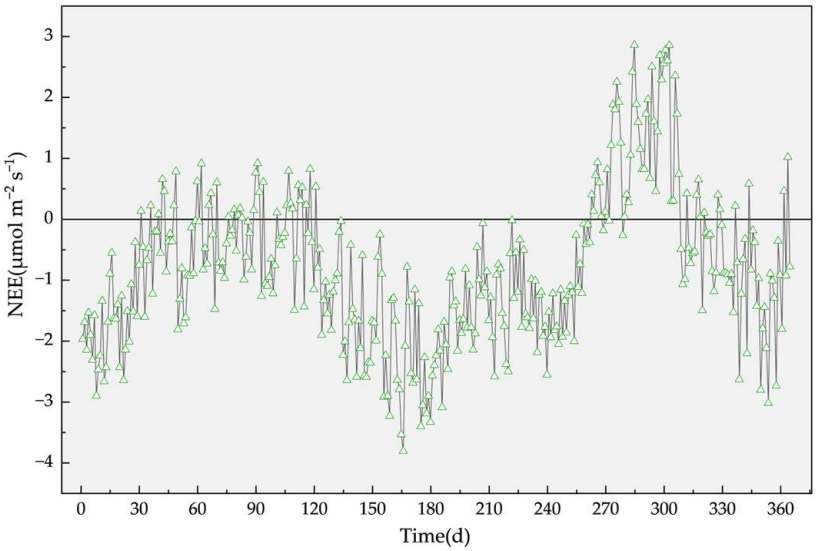

Figure 7. Annual variation in net ecosystem exchange (NEE) at Haihu Wetland Park, Xining, northeastern Qinghai–Tibetan Plateau. Negative values indicate net CO_2 uptake (carbon sink), and positive values indicate net CO_2 release (carbon source).

3.4. Dynamics of Environmental Factors

In 2023, radiation, temperature, and soil moisture exhibited marked seasonal variability at the site (Figure 8). PPFD increased from spring to midsummer and then declined, forming an inverted V-shaped annual trajectory. Monthly mean PPFD reached its maximum in July (574.3 μmol m^{-2} s^{-1}) and remained much lower in winter (≈200 μmol m^{-2} s^{-1} on average). The PPFD record also showed intermittent short-term excursions from the seasonal curve, with several of these occurring during periods with precipitation and greater cloudiness. Air temperature followed a coherent annual cycle. The mean T_a was 8.24 °C. The monthly maximum of daily T_{max} occurred in July (31.98 °C), and the monthly minimum of daily T_{min} occurred in January (−28.6 °C). T_{s5} varied in phase with T_a, peaking in July (22.93 °C) and reaching a minimum in January (−5.1 °C). Across the year, T_{s5} was slightly higher than T_a, indicating a small but persistent offset between near-surface soil and air temperatures. Curve fits to the temperature indices yielded a unimodal seasonal form, characterized by spring warming, a summer peak, and cooling toward winter. SWC also showed a clear seasonal progression. Values were relatively high but more variable in spring and summer, increased into autumn, and peaked around DOY ~300 before decreasing to winter minima. Precipitation occurred mainly in late spring and early summer, whereas winter was largely dry. The flux-tower rain gauge recorded 121.8 mm of precipitation in 2023, with rainfall concentrated in a limited seasonal window and occurring primarily as discrete, high-intensity events.

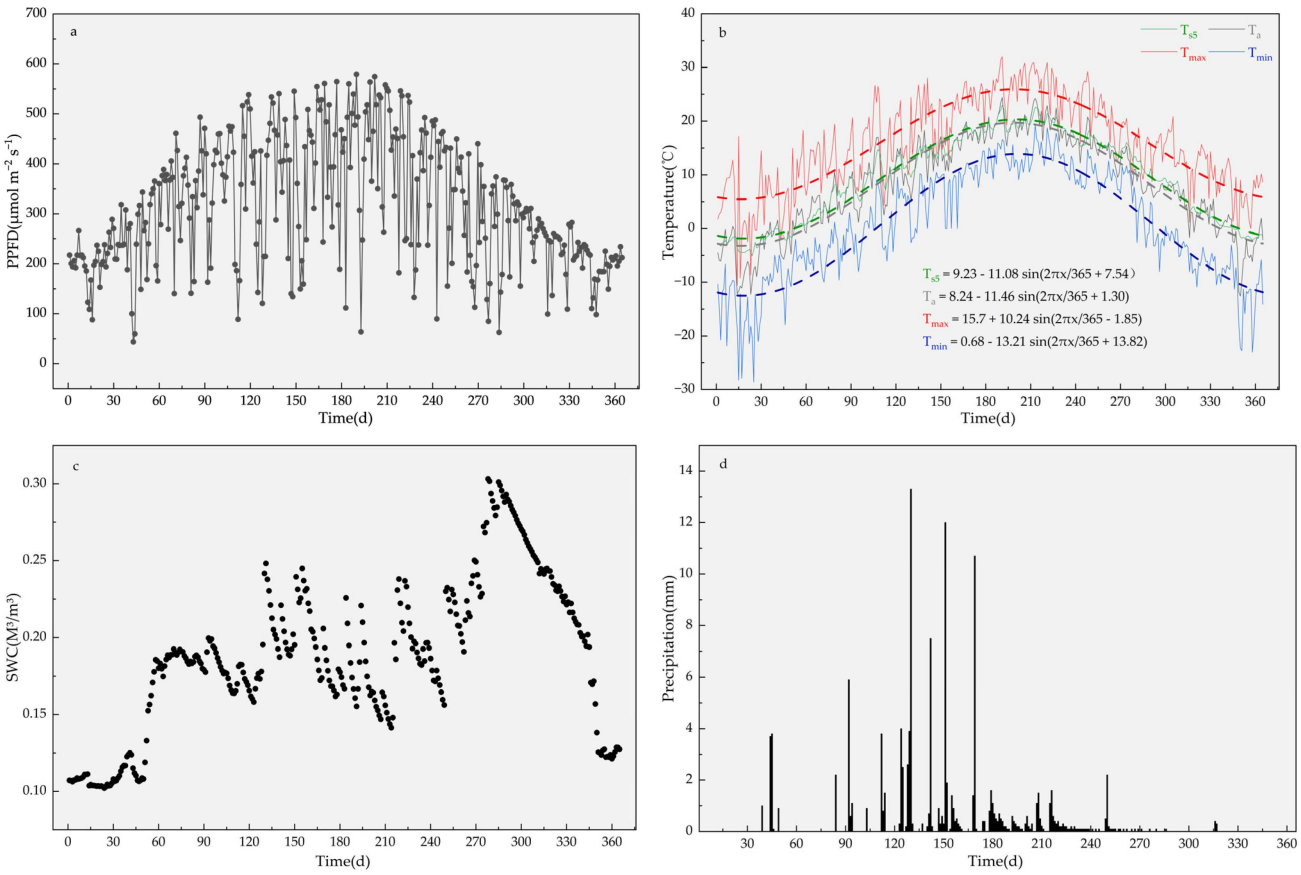

Figure 8. Annual dynamics of environmental variables at Haihu Wetland Park, Xining, northeastern Qinghai–Tibetan Plateau: (**a**) photosynthetic photon flux density (PPFD); (**b**) air temperature (T_a), daily maximum air temperature (T_{max}), daily minimum air temperature (T_{min}), and soil temperature at 5 cm depth (T_{s5}); (**c**) volumetric soil water content (SWC); and (**d**) precipitation.

4. Discussion

4.1. Mechanisms of Environmental Controls on NEE, GPP, and Re

Carbon flux dynamics in urban ecosystems are jointly influenced by natural and anthropogenic factors, among which water and thermal conditions are generally regarded as the key environmental drivers regulating carbon exchange processes [51]. Although the study area is located within an urban setting, its climatic conditions and ecological processes still exhibit pronounced characteristics of alpine environments. Therefore, carbon exchange processes in this urban wetland can be reasonably compared with those observed in alpine grassland and wetland ecosystems. Pearson correlation analysis based on daily means (n = 365) revealed varying associations between environmental variables and carbon flux components (Figure 9a). GPP was positively correlated with Re (r = 0.81, $p < 0.001$). In contrast, NEE was weakly but significantly negatively correlated with GPP (r = −0.32, $p < 0.001$), indicating that higher GPP tended to be associated with stronger net CO_2 uptake under our sign convention. In contrast, Re showed a weak positive correlation with NEE (r = 0.30), suggesting that respiration may partially offset increases in net uptake associated with higher GPP. This offset effect is consistent with the relatively weak pairwise correlations of NEE to individual environmental factors, as NEE represents the integrated outcome of the combined responses of GPP and Re [52,53]. Among the examined environmental variables, temperature showed the strongest associations with the carbon flux components [54,55]. Both T_a and T_{s5} were significantly and positively correlated with GPP and Re. Compared with T_a, T_{s5} exhibited stronger correlations with GPP (r = 0.79) and Re

(r = 0.71), which is consistent with previous findings that soil temperature is often more closely linked to carbon flux dynamics. These results further suggest the importance of soil thermal conditions for variations in carbon flux components [56]. PPFD showed positive correlations with GPP and Re and a weak negative correlation with NEE; however, the correlation coefficients were relatively low, indicating limited explanatory power in carbon flux components. This pattern may be attributed to the generally sufficient solar radiation conditions in alpine regions, suggesting that PPFD may not be a primary limiting factor for GPP at the daily scale in the study area. Precipitation exhibited weak and non-significant correlations with carbon flux components ($|r| < 0.15$), whereas SWC showed moderate positive correlations with GPP (r = 0.44), Re (r = 0.62), and NEE (r = 0.44). This difference likely reflects the constrained evapotranspiration capacity in alpine environments, where the impacts of short-term precipitation events on soil moisture dynamics and vegetation physiological processes tend to be delayed [57]. In contrast, SWC more directly reflects soil microbial activity and root physiological processes, and may therefore be more closely associated with variations in flux components.

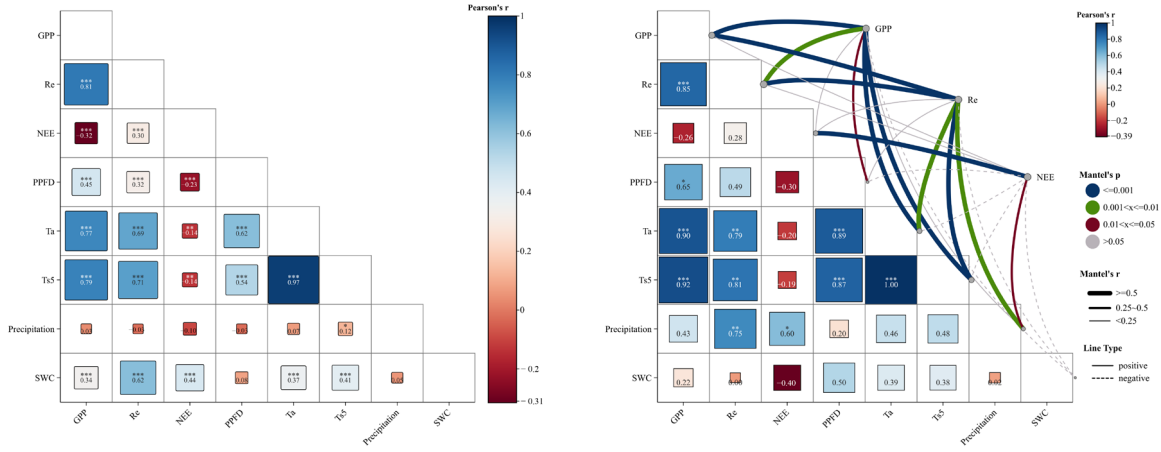

(**a**) (**b**)

Figure 9. Relationships between environmental variables and carbon flux components at Haihu Wetland Park, Xining, northeastern Qinghai–Tibetan Plateau. (**a**) Pearson correlation matrix based on daily mean values (n = 365). Significance levels are denoted as * $p < 0.05$, ** $p < 0.01$, and *** $p < 0.001$. (**b**) Mantel test results based on monthly aggregated data (n = 12). Pearson significance levels are denoted as * for $p < 0.05$, ** for $p < 0.01$, and *** for $p < 0.001$. Line colors indicate Mantel test significance (blue, $p \leq 0.001$; green, $0.001 < p \leq 0.01$; red, $0.01 < p \leq 0.05$; grey, $p > 0.05$); line types indicate the direction of association (solid, positive; dashed, negative); and line widths indicate Mantel r values ($r \geq 0.5$, $0.25 \leq r < 0.5$, $r < 0.25$). Euclidean distance matrices were used for both carbon flux components and environmental variables.

To reduce high-frequency noise and emphasize seasonal covariation, we conducted Mantel tests on monthly aggregated data (n = 12) (Figure 9b), which evaluate the correspondence between distance matrices of carbon flux components and environmental variables. The Mantel results further supported a dominant thermal control, with additional precipitation-related effects at the monthly scale. Specifically, GPP exhibited significant Mantel associations with T_a (Mantel's r = 0.733, p = 0.001) and T_{s5} (Mantel's r = 0.782, p = 0.001), whereas precipitation and SWC were not significant ($p > 0.05$), which may indicate that moisture effects were more apparent at the daily scale than in month-to-month distance-based comparisons. Re also showed significant Mantel correlations with T_{s5} (r = 0.573, p = 0.001) and T_a (r = 0.539, p = 0.004), and additionally with precipitation (r = 0.513, p = 0.005), implying that precipitation may modulate respiration at the monthly

scale, likely via changes in substrate availability and moisture conditions. In contrast, NEE showed a significant Mantel relationship only with precipitation (r = 0.427, $p = 0.045$) while associations with temperature, PPFD, and SWC were not significant ($p > 0.05$), consistent with NEE being a net balance variable that integrates opposing responses of GPP and Re. Taken together, the daily-scale Pearson results and monthly-scale Mantel tests suggest that temperature is the dominant control on GPP and Re, whereas precipitation can additionally modulate respiration and the net carbon balance at the monthly scale. This pattern is broadly consistent with the hydrothermal coupling mechanism reported for alpine ecosystems [58].

In addition to hydrothermal controls, the biogeochemical status of urban wetland soils—shaped by macro- and micronutrient availability, trace metal inputs, and enzyme-mediated microbial processes—may influence carbon turnover and soil CO_2 emissions [59]. However, because nutrient concentrations, trace metals, and soil enzyme activities were not measured in this study, these mechanisms cannot be directly tested with our current dataset and should be considered as plausible explanations rather than quantified drivers. Future work combining flux observations with stratified soil sampling across dominant land-cover types within the footprint (e.g., woodland, grassland, and wetland patches) and analyses of nutrients, metal contents, and key carbon-degrading enzymes would help to evaluate whether biogeochemical "hotspots" contribute to the observed seasonal source–sink transitions.

Pearson correlation analysis indicated that temperature and SWC were key environmental factors associated with variability in carbon flux components in the study area, while Mantel tests further showed stronger associations between T_a, T_{s5}, and the flux components. In addition, nonlinear fits between T_a, T_{s5}, and carbon flux components provided quantitative support for temperature as a major correlate of flux variability. As shown in Figure 10, GPP exhibited a pronounced sigmoidal (S-shaped) response to both T_a and T_{s5} [60]. When T_a or T_{s5} was below 5 °C, GPP was strongly suppressed and approached its minimum values, indicating limitation under low temperatures. In the intermediate range (5–15 °C), GPP increased rapidly, consistent with enhanced vegetation physiological activity at warmer temperatures. When T_a or T_{s5} exceeded 15 °C, GPP entered a high-temperature saturation phase, during which further temperature increases produced only marginal increases in GPP. This non-linear temperature response pattern, in which GPP reaches an optimum and saturates or declines at high temperatures, has been widely observed across eddy covariance flux towers, where the apparent optimum air temperature for photosynthesis provides a key constraint on GPP responses to thermal conditions. Re responses to T_a and T_{s5} followed a quadratic relationship, showing broadly similar trends to GPP but with more gradual increases and an apparent leveling-off tendency at higher temperatures. In contrast, the relationships between NEE and T_a or T_{s5} exhibited a distinct nonlinear optimum pattern: with increasing temperature, NEE did not change monotonically but instead became least negative (approaching zero or becoming positive) within an intermediate temperature range, indicating weakened sink strength and, in some cases, a temporary shift toward a CO_2 source. This nonlinear response of NEE may reflect differences in the temperature sensitivities of GPP and Re [61]. Under low-temperature conditions, both GPP and Re were limited and NEE was generally negative, indicating net CO_2 uptake under our sign convention. As temperature increased, Re appeared to be more temperature-sensitive than GPP [10,62], and enhanced respiration partially offset carbon uptake, leading to a weakened sink or a temporary source. At higher temperatures, increases in photosynthetic capacity were associated with periods when GPP exceeded Re, and the ecosystem reverted to a net CO_2 sink. This nonlinear temperature dependence of NEE was also evident at the annual scale. During DOY 150–270 (approximately June–September), T_a and T_{s5} reached

relatively high levels; however, NEE became less negative during this period. Together, these results suggest that temperature influences seasonal transitions between CO_2 sink and source states primarily by altering the relative magnitudes of GPP and Re, rather than through a simple linear enhancement of fluxes.

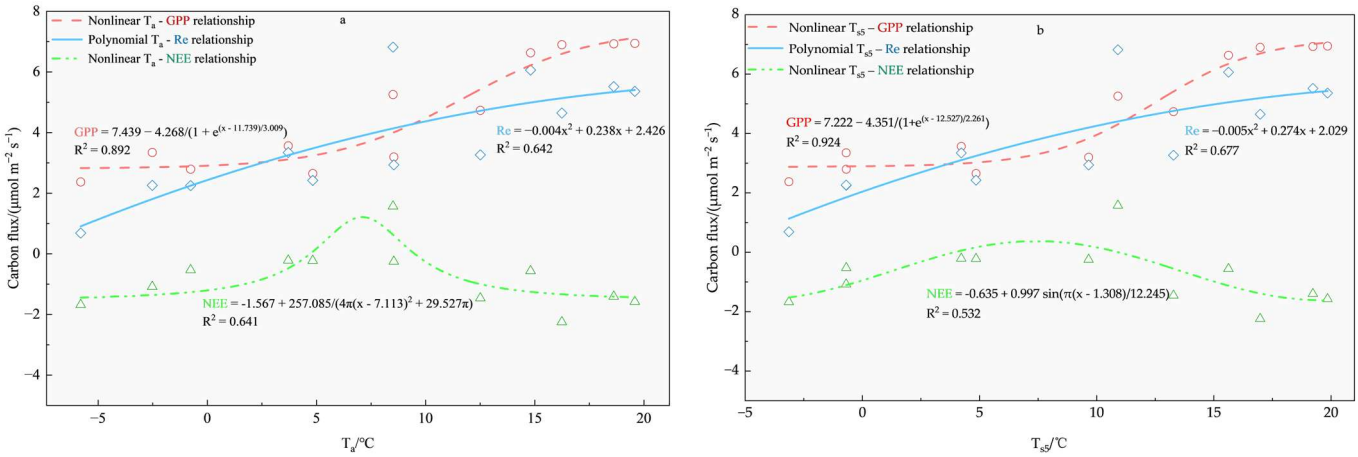

(**a**) (**b**)

Figure 10. Relationships between (**a**) air temperature (T_a) and (**b**) soil temperature at 5 cm depth (T_{s5}) and gross primary productivity (GPP), ecosystem respiration (Re), and net ecosystem exchange (NEE) at Haihu Wetland Park, Xining, northeastern Qinghai–Tibetan Plateau. Curves represent fitted nonlinear relationships. Red circles represent GPP, blue diamonds represent Re, and green triangles represent NEE.

4.2. Carbon Source-Sink Characteristics Analysis

Based on the partitioned fluxes, monthly totals (g C m^{-2} $month^{-1}$) of GPP, Re, and NEE were calculated for 2023 (Figure 11). GPP was substantially higher during the growing season (June–October) but remained low during the non-growing season. Notably, Re maintained measurable values even in winter, suggesting persistent biological activity of soil microorganisms under cold conditions [59]. Re reached its maximum monthly total in October (249.2 g C m^{-2} $month^{-1}$), substantially exceeding summer values, which is consistent with enhanced ecosystem respiration associated with litter inputs and decomposition processes in autumn [63]. NEE was negative in most months, suggesting that the study area functioned as a carbon sink (net CO_2 uptake) for much of the year. Overall, the cumulative net carbon uptake in 2023 was 292.25 g C m^{-2} yr^{-1}, indicating that the ecosystem acted as a strong annual carbon sink. This sink strength was substantially greater than that reported for alpine shrublands in northern Tibet (5.56 g C m^{-2} yr^{-1}) [64], likely reflecting differences in ecosystem type, surface characteristics, and soil organic carbon content within the flux footprint. Clear month-to-month transitions between carbon sink and carbon source states were also evident. From January to August, the ecosystem acted as a carbon sink, accounting for 88.5% of the annual net uptake, with the strongest monthly uptake occurring in June (68.1 g C m^{-2} $month^{-1}$), primarily driven by high GPP in early summer. The ecosystem shifted to a carbon source in September, and carbon release peaked in October (50.18 g C m^{-2} $month^{-1}$). This reversal likely reflects a much stronger increase in Re than in GPP during autumn [65], which reversed the carbon balance and caused the transition from a carbon sink to a carbon source. In November and December, the ecosystem shifted back to a carbon sink, coinciding with decreased Re, leading to another change in the sink–source behavior.

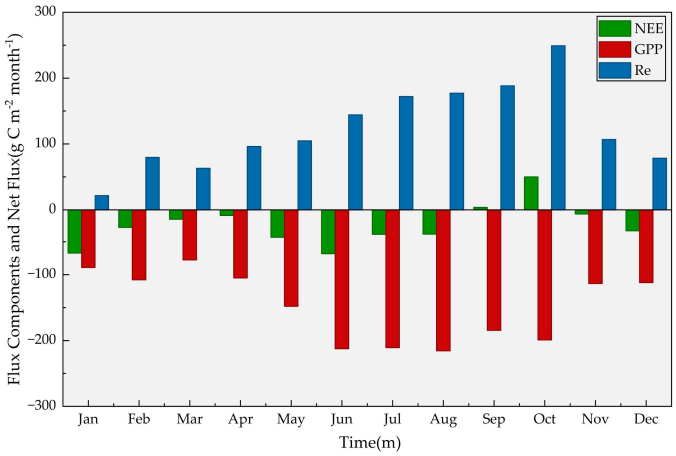

Figure 11. Monthly cumulative sums of gross primary productivity (GPP), ecosystem respiration (Re), and net ecosystem exchange (NEE) at Haihu Wetland Park, Xining, northeastern Qinghai–Tibetan Plateau. Negative NEE values indicate net carbon uptake, whereas positive values indicate net carbon release.

5. Conclusions

This study used eddy covariance observations from Haihu Wetland Park to quantify the temporal dynamics of GPP, Re, and NEE in an urban wetland ecosystem in Xining, and to examine their associations with key environmental drivers. The main conclusions are as follows:

(1) Figures 2–7 show that GPP, Re, and NEE exhibited pronounced diurnal and seasonal variability. At the diurnal scale, both GPP and Re displayed generally unimodal patterns, with higher peak values during the growing season than during the non-growing season, while NEE was characterized by nocturnal CO_2 release and daytime uptake. At the annual scale, GPP and Re followed unimodal seasonal trajectories, whereas NEE exhibited a bimodal pattern, indicating clear seasonal transitions between net CO_2 source and sink states.

(2) As shown in Figures 8–10, At the daily scale, Pearson correlation analysis indicated that temperature (T_a and T_{s5}) and SWC were the strongest correlates of variability in carbon flux components, whereas PPFD showed moderate associations and precipitation was weak. At the monthly scale, Mantel tests indicated strong thermal associations with GPP and Re (T_a and T_{s5}), and precipitation was additionally associated with Re and NEE, while SWC was not significant. Both T_a and T_{s5} were significantly and positively correlated with GPP and Re, with stronger correlations for T_{s5}, suggesting that soil temperature (T_{s5}) may better track variability in ecosystem carbon exchange than air temperature (T_a). Nonlinear fits were consistent with these patterns. GPP exhibited a sigmoidal response to both T_a and T_{s5}, showing strong suppression at low temperatures, a rapid increase over an intermediate temperature range, and diminishing gains at higher temperatures. Re increased nonlinearly with T_a and T_{s5} but more gradually, while NEE exhibited a nonlinear optimum response. Overall, carbon exchange at this site was most strongly associated with combined hydrothermal conditions, and seasonal source–sink transitions were broadly consistent with seasonal temperature dynamics.

(3) According to Figure 11, the study area functioned overall as a net carbon sink, with an annual net carbon uptake of 292.25 g C m^{-2} yr^{-1}. Net carbon sequestration was concentrated between January and August, whereas the ecosystem temporarily shifted to a net carbon source during September–October when increases in Re outpaced those in GPP.

We note that our inference on hydrothermal regulation is based on the environmental variables measured at the flux tower; unmeasured biogeochemical factors (e.g., nutrients, metals, and enzyme activities) may additionally modulate respiration dynamics in this urban wetland and therefore warrant further investigation. It should also be acknowledged that the hydrothermal controls and annual carbon sink behavior identified in this study are derived from observations at a single urban wetland site over a single year. Interannual climate variability, extreme weather events, and site-specific factors related to urban management and land-cover composition may lead to different carbon flux responses in other years or locations. Accordingly, while our results provide robust process-level evidence for hydrothermal regulation at this site, their generalization to other urban wetlands or longer temporal scales should be made with caution. Multi-year and multi-site eddy covariance observations are required to further evaluate the consistency and broader applicability of these patterns. From an applied perspective, this study provides empirical constraints and process-level evidence for urban wetland carbon flux research, contributing to more accurate carbon budget estimation, improved interpretation of eddy covariance observations, and enhanced understanding of carbon source–sink dynamics in urban wetland ecosystems, particularly in high-altitude regions.

Author Contributions: Conceptualization, J.L.; methodology, J.L., X.M. and X.W.; investigation, J.L. and Y.Y.; resources, X.S. and S.X.; data curation, J.L. and J.Z.; writing—original draft preparation, J.L.; writing—review and editing, X.M., L.Z. and H.Y.; visualization, J.L. and Y.Y.; supervision, X.M.; funding acquisition, X.M. All authors have read and agreed to the published version of the manuscript.

Funding: This research was supported by the Natural Science Foundation of Qinghai Provincial Department of Science and Technology ("Research and demonstration of ultra-low-temperature operation technologies for high-altitude constructed wetlands", Grant Number: 2024-ZJ-910) and the Leading Talent Program of the Qinghai Provincial High-End Innovation and Entrepreneurship Program.

Institutional Review Board Statement: Not applicable.

Informed Consent Statement: Not applicable.

Data Availability Statement: All flux data used in this study were obtained from the eddy-covariance flux tower at the Huangshui Park Station, others are contained within the article, further inquiries can be directed to the corresponding author.

Acknowledgments: We thank the reviewers for their constructive comments and suggestions to improve the early version of this paper. We also thank the Wetland Ecological Processes Research Group, School of Geographical Sciences, Qinghai Normal University, for their support, and the Management and Service Center of the Huangshui National Wetland Park, Xining, Qinghai, for providing the eddy-covariance flux tower data from the Huangshui Park Station.

Conflicts of Interest: The authors declare no conflicts of interest.

Abbreviations

The following abbreviations are used in this manuscript:

GPP	Gross Primary Productivity
Re	Ecosystem Respiration
NEE	Net Ecosystem Exchange
T_a	Air Temperature
T_{s5}	Soil Temperature at 5 cm (Depth)
T_{max}	Monthly Maximum of Daily T_{max}
T_{min}	Monthly Minimum of Daily T_{min}
SWC	Volumetric Soil Water Content

PPFD	Photosynthetic Photon Flux Density
EC	Eddy Covariance
WPL	Webb–Pearman–Leuning (Correction)
Rn	Net Radiation
G	Soil Heat Flux
S	Canopy Heat Storage
Q	Other Minor Storage Terms
H	Sensible Heat Flux
LE	Latent Heat Flux

References

1. Mitsch, W.J.; Bernal, B.; Nahlik, A.M.; Mander, Ü.; Zhang, L.; Anderson, C.J.; Jørgensen, S.E.; Brix, H. Wetlands, carbon, and climate change. *Landsc. Ecol.* **2013**, *28*, 583–597. [CrossRef]
2. Liu, J.Y.; Li, J.; Qin, K.Y.; Zhou, Z.X.; Yang, X.N.; Li, T. Changes in land uses and ecosystem services under multi-scenario simulations. *Sci. Total Environ.* **2017**, *586*, 522–526. [CrossRef] [PubMed]
3. Seto, K.C.; Güneralp, B.; Hutyra, L.R. Global forecasts of urban expansion to 2030 and direct impacts on biodiversity and carbon pools. *Proc. Natl. Acad. Sci. USA* **2012**, *109*, 16083–16088. [CrossRef] [PubMed]
4. Jantz, P.; Goetz, S.; Jantz, C. Urbanization and the loss of resource lands in the Chesapeake Bay watershed. *Environ. Manag.* **2005**, *36*, 808–825. [CrossRef] [PubMed]
5. Grimm, N.B.; Faeth, S.H.; Golubiewski, N.E.; Redman, C.L.; Wu, J.; Bai, X.; Briggs, J.M. Global change and the ecology of cities. *Science* **2008**, *319*, 756–760. [CrossRef]
6. Mitsch, W.J.; Gosselink, J.G. *Wetlands*, 4th ed.; John Wiley & Sons: Hoboken, NJ, USA, 2007.
7. Faulkner, S. Urbanization impacts on the structure and function of forested wetlands. *Urban Ecosyst.* **2004**, *7*, 89–106. [CrossRef]
8. Finlayson, M.; Cruz, R.D.; Davidson, N.; Alder, J.; Cork, S.; Groot, R.S.; Lévêque, C.; Milton, G.R.; Peterson, G.; Pritchard, D.; et al. *Millennium Ecosystem Assessment: Ecosystems and Human Well-Being: Wetlands and Water Synthesis*; World Resources Institute: Washington, DC, USA, 2005.
9. Zedler, J.B.; Kercher, S. Wetland resources: Status, trends, ecosystem services, and restorability. *Annu. Rev. Environ. Resour.* **2005**, *30*, 39–74. [CrossRef]
10. Baldocchi, D. Measuring fluxes of trace gases and energy between ecosystems and the atmosphere—The state and future of the eddy covariance method. *Glob. Change Biol.* **2014**, *20*, 3600–3609. [CrossRef]
11. Herig Coimbra, P.H.; Loubet, B.; Laurent, O.; Bignotti, L.; Lozano, M.; Ramonet, M. Eddy covariance with slow-response greenhouse gas analysers on tall towers: Bridging atmospheric and ecosystem greenhouse gas networks. *Atmos. Meas. Tech.* **2024**, *17*, 6625–6645. [CrossRef]
12. Falge, E.; Tenhunen, J.; Baldocchi, D.; Aubinet, M.; Bakwin, P.; Berbigier, P.; Bernhofer, C.; Bonnefond, J.; Burba, G.; Clement, R.; et al. Phase and amplitude of ecosystem carbon release and uptake potentials as derived from FLUXNET measurements. *Agric. For. Meteorol.* **2002**, *113*, 75–95. [CrossRef]
13. Gilmanov, T.G.; Soussana, J.F.; Aires, A.; Allard, V.; Ammann, C.; Balzarolo, M.; Barcza, C.; Bernhofer, C.; Campbell, C.L.; Cernusca, A.; et al. Partitioning European grassland net ecosystem CO_2 exchange into gross primary productivity and ecosystem respiration using light response function analysis. *Agric. Ecosyst. Environ.* **2007**, *121*, 93–120. [CrossRef]
14. Baldocchi, D.; Falge, E.; Gu, L.; Olson, R.; Hollinger, D.; Running, S.; Anthoni, P.; Bernhofer, C.; Davis, K.; Evans, R.; et al. FLUXNET: A New Tool to Study the Temporal and Spatial Variability of Ecosystem-Scale Carbon Dioxide, Water Vapor, and Energy Flux Densities. *Bull. Am. Meteorol. Soc.* **2001**, *82*, 2415–2434. [CrossRef]
15. Baldocchi, D. 'Breathing' of the terrestrial biosphere: Lessons learned from a global network of carbon dioxide flux measurement systems. *Aust. J. Bot.* **2008**, *56*, 1–26. [CrossRef]
16. Ciais, P.; Reichstein, M.; Viovy, N.; Granier, A.; Ogée, J.; Allard, V.; Aubinet, M.; Buchmann, N.; Bernhofer, C.; Carrara, A.; et al. Europe-wide reduction in primary productivity caused by the heat and drought in 2003. *Nature* **2005**, *437*, 529–533. [CrossRef] [PubMed]
17. Valentini, R.; Matteucci, G.; Dolman, A.J.; Schulze, E.D.; Rebmann, C.; Moors, E.J.; Granier, A.; Gross, P.; Jensen, N.O.; Pilegaard, K.; et al. Respiration as the main determinant of carbon balance in European forests. *Nature* **2000**, *404*, 861–865. [CrossRef]
18. Raich, J.W.; Schlesinger, W.H. The global carbon dioxide flux in soil respiration and its relationship to vegetation and climate. *Tellus B* **1992**, *44*, 81–99. [CrossRef]
19. Zhu, X.J.; Yu, G.R.; He, H.L.; Wang, Q.F.; Chen, Z.; Gao, Y.N.; Zhang, Y.P.; Zhang, J.H.; Yan, J.H.; Wang, H.M.; et al. Geographical statistical assessments of carbon fluxes in terrestrial ecosystems of China: Results from upscaling network observations. *Glob. Planet. Change* **2014**, *118*, 52–61. [CrossRef]

20. Schimel, D.S. Terrestrial ecosystems and the carbon cycle. *Glob. Change Biol.* **1995**, *1*, 77–91. [CrossRef]
21. Li, X.; Wahlroos, O.; Haapanala, S.; Pumpanen, J.; Vasander, H.; Ojala, A.; Vesala, T.; Mammarella, I. Carbon dioxide and methane fluxes from different surface types in a created urban wetland. *Biogeosciences* **2020**, *17*, 3409–3425. [CrossRef]
22. Du, F.; Chen, Z.; Li, X.; Liu, J.; Kan, X.; Wang, Y.; Liu, X.; Yao, D. Spatial patterns and controlling mechanisms of CO_2 fluxes across China's diverse wetlands based on eddy covariance measurements. *Land* **2025**, *14*, 1629. [CrossRef]
23. Yao, H.; Peng, H.; Hong, B.; Guo, Q.; Ding, H.; Hong, Y.; Zhu, Y.; Cai, C.; Chi, J. Environmental controls on multi-scale dynamics of net carbon dioxide exchange from an alpine peatland on the eastern Qinghai–Tibet Plateau. *Front. Plant Sci.* **2021**, *12*, 791343. [CrossRef] [PubMed]
24. Shahan, J.; Chu, H.; Windham-Myers, L.; Maiyah, M.; Carlin, J.; Eichelmann, E.; Stuart-Haentjens, E.; Bergamaschi, B.; Nakatsuka, K.; Sturtevant, C.; et al. Combining eddy covariance and chamber methods to better constrain CO_2 and CH_4 fluxes across a heterogeneous restored tidal wetland. *J. Geophys. Res. Biogeosci.* **2022**, *127*, e2022JG007112. [CrossRef]
25. Valach, A.C.; Kasak, K.; Hemes, K.S.; Anthony, T.L.; Dronova, I.; Taddeo, S.; Silver, W.L.; Szutu, D.; Verfaillie, J.; Baldocchi, D.D. Productive wetlands restored for carbon sequestration quickly become net CO_2 sinks with site-level factors driving uptake variability. *PLoS ONE* **2021**, *16*, e0248398. [CrossRef] [PubMed]
26. Horne, J.P.; Richardson, S.J.; Murphy, S.L.; Kenion, H.C.; Haupt, B.J.; Ahlswede, B.J.; Miles, N.L.; Davis, K.J. The INFLUX network—Eddy covariance in and around an urban environment. *Earth Syst. Sci. Data* **2026**, *18*, 823–843. [CrossRef]
27. Kato, T.; Yamada, K.; Tang, Y.; Yoshida, N.; Wada, E. Stable carbon isotopic evidence of methane consumption and production in three alpine ecosystems on the Qinghai–Tibetan Plateau. *Atmos. Environ.* **2013**, *77*, 338–347. [CrossRef]
28. Wei, D.; Xu, R.; Tarchen, T.; Dai, D.; Wang, Y.; Wang, Y. Revisiting the role of CH_4 emissions from alpine wetlands on the Tibetan Plateau: Evidence from two in situ measurements at 4758 and 4320 m above sea level. *J. Geophys. Res. Biogeosci.* **2015**, *120*, 1741–1750. [CrossRef]
29. Zhang, Y.; Li, C.; Trettin, C.C.; Li, H.; Sun, G. An integrated model of soil, hydrology, and vegetation for carbon dynamics in wetland ecosystems. *Glob. Biogeochem. Cycles* **2002**, *16*, 1061. [CrossRef]
30. Liu, X.; Chen, B. Climatic warming in the Tibetan Plateau during recent decades. *Int. J. Climatol.* **2000**, *20*, 1729–1742. [CrossRef]
31. Xue, Z.; Zhang, Z.; Lu, X.; Zou, Y.; Lu, Y.; Jiang, M.; Tong, S.; Zhang, K. Predicted areas of potential distributions of alpine wetlands under different scenarios in the Qinghai-Tibetan Plateau, China. *Glob. Planet. Change* **2014**, *123*, 77–85. [CrossRef]
32. Tong, X.; Meng, P.; Zhang, J.; Li, J.; Zheng, N.; Huang, H. Ecosystem Carbon Exchange over a Warm-Temperate Mixed Plantation in the Lithoid Hilly Area of the North China. *Atmos. Environ.* **2012**, *49*, 257–267. [CrossRef]
33. Cole, J.J.; Prairie, Y.T.; Caraco, N.F.; McDowell, W.H.; Tranvik, L.J.; Striegl, R.G.; Duarte, C.M.; Kortelainen, P.; Downing, J.A.; Middelburg, J.J.; et al. Plumbing the Global Carbon Cycle: Integrating Inland Waters into the Terrestrial Carbon Budget. *Ecosystems* **2007**, *10*, 172–185. [CrossRef]
34. Mao, X.; Wei, X.; Chen, Q.; Liu, F.; Tao, Y.; Zhang, Z. An E_{CPS} framework based assessment on wetland restoration of the Huangshui National Wetland Park in Qinghai province, China. *Geogr. Res.* **2019**, *38*, 760–771. (In Chinese) [CrossRef]
35. Kljun, N.; Calanca, P.; Rotach, M.W.; Schmid, H.P. A simple two-dimensional parameterisation for Flux Footprint Prediction (FFP). *Geosci. Model Dev.* **2015**, *8*, 3695–3713. [CrossRef]
36. Schuepp, P.H.; Leclerc, M.Y.; Macpherson, J.I.; Desjardins, R.L. Footprint prediction of scalar fluxes from analytical solutions of the diffusion equation. *Bound.-Layer Meteorol.* **1990**, *50*, 355–373. [CrossRef]
37. Kormann, R.; Meixner, F.X. An Analytical Footprint Model For Non-Neutral Stratification. *Bound.-Layer Meteorol.* **2001**, *99*, 207–224. [CrossRef]
38. Baldocchi, D.D. Assessing the eddy covariance technique for evaluating carbon dioxide exchange rates of ecosystems: Past, present and future. *Glob. Change Biol.* **2003**, *9*, 479–492. [CrossRef]
39. Wilson, K.; Goldstein, A.; Falge, E.; Aubinet, M.; Baldocchi, D.; Berbigier, P.; Bernhofer, C.; Ceulemans, R.; Dolman, H.; Field, C.; et al. Energy balance closure at FLUXNET sites. *Agric. For. Meteorol.* **2002**, *113*, 223–243. [CrossRef]
40. Webb, E.K.; Pearman, G.I.; Leuning, R. Correction of Flux Measurements for Density Effects Due to Heat and Water-Vapor Transfer. *Q. J. R. Meteorol. Soc.* **1980**, *106*, 85–100. [CrossRef]
41. Moncrieff, J.B.; Massheder, J.M.; de Bruin, H.; Elbers, J.; Friborg, T.; Heusinkveld, B.; Kabat, P.; Scott, S.; Soegaard, H.; Verhoef, A. A system to measure surface fluxes of momentum, sensible heat, water vapour and carbon dioxide. *J. Hydrol.* **1997**, *188–189*, 589–611. [CrossRef]
42. Wohlfahrt, G.; Hörtnagl, L.; Hammerle, A.; Graus, M.; Hansel, A. Measuring eddy covariance fluxes of ozone with a slow-response analyser. *Atmos. Environ.* **2009**, *43*, 4570–4576. [CrossRef]
43. Foken, T.; Wichura, B. Tools for quality assessment of surface-based flux measurements. *Agric. For. Meteorol.* **1996**, *78*, 83–105. [CrossRef]
44. Fratini, G.; Mauder, M. Towards a consistent eddy-covariance processing: An intercomparison of EddyPro and TK3. *Atmos. Meas. Tech.* **2014**, *7*, 2273–2281. [CrossRef]

45. Papale, D.; Reichstein, M.; Aubinet, M.; Canfora, E.; Bernhofer, C.; Kutsch, W.; Longdoz, B.; Rambal, S.; Valentini, R.; Vesala, T.; et al. Towards a standardized processing of Net Ecosystem Exchange measured with eddy covariance technique: Algorithms and uncertainty estimation. *Biogeosciences* **2006**, *3*, 571–583. [CrossRef]
46. Barr, A.G.; Richardson, A.D.; Hollinger, D.Y.; Papale, D.; Arain, M.A.; Black, T.A.; Bohrer, G.; Dragoni, D.; Fischer, M.L.; Gu, L.; et al. Use of change-point detection for friction–velocity threshold evaluation in eddy-covariance studies. *Agric. For. Meteorol.* **2013**, *171–172*, 31–45. [CrossRef]
47. Lloyd, J.; Taylor, J.A. On the Temperature Dependence of Soil Respiration. *Funct. Ecol.* **1994**, *8*, 315–323. [CrossRef]
48. Falge, E.; Baldocchi, D.; Olson, R.; Anthoni, P.; Aubinet, M.; Bernhofer, C.; Burba, G.; Ceulemans, R.; Clement, R.; Dolman, H.; et al. Gap filling strategies for defensible annual sums of net ecosystem exchange. *Agric. For. Meteorol.* **2001**, *107*, 43–69. [CrossRef]
49. Foken, T.; Göockede, M.; Mauder, M.; Mahrt, L.; Amiro, B.; Munger, W. Post-field data quality control. In *Handbook of Micrometeorology: A Guide for Surface Flux Measurement and Analysis*; Lee, X., Massman, W., Law, B., Eds.; Springer: Dordrecht, The Netherlands, 2005; pp. 181–208. [CrossRef]
50. Lasslop, G.; Reichstein, M.; Papale, D.; Richardson, A.D.; Arneth, A.; Barr, A.; Stoy, P.; Wohlfahrt, G. Separation of net ecosystem exchange into assimilation and respiration using a light response curve approach: Critical issues and global evaluation. *Glob. Change Biol.* **2010**, *16*, 187–208. [CrossRef]
51. Saito, M.; Kato, T.; Tang, Y. Temperature controls ecosystem CO_2 exchange of an alpine meadow on the northeastern Tibetan Plateau. *Glob. Change Biol.* **2009**, *15*, 221–228. [CrossRef]
52. Reichstein, M.; Falge, E.; Baldocchi, D.; Papale, D.; Aubinet, M.; Berbigier, P.; Bernhofer, C.; Buchmann, N.; Gilmanov, T.; Granier, A.; et al. On the separation of net ecosystem exchange into assimilation and ecosystem respiration: Review and improved algorithm. *Glob. Change Biol.* **2005**, *11*, 1424–1439. [CrossRef]
53. Zhao, L.; Li, J.; Xu, S.; Zhou, H.; Li, Y.; Gu, S.; Zhao, X. Seasonal variations in carbon dioxide exchange in an alpine wetland meadow on the Qinghai-Tibetan Plateau. *Biogeosciences* **2010**, *7*, 1207–1221. [CrossRef]
54. Kato, T.; Tang, Y.; Gu, S.; Cui, X.; Hirota, M.; Du, M.; Li, Y.; Zhao, X.; Oikawa, T. Carbon dioxide exchange between the atmosphere and an alpine meadow ecosystem on the Qinghai–Tibetan Plateau, China. *Agric. For. Meteorol.* **2004**, *124*, 121–134. [CrossRef]
55. Piao, S.; Fang, J.; Ciais, P.; Peylin, P.; Huang, Y.; Sitch, S.; Wang, T. The carbon balance of terrestrial ecosystems in China. *Nature* **2009**, *458*, 1009–1013. [CrossRef] [PubMed]
56. Lin, X.; Zhang, Z.; Wang, S.; Hu, Y.; Xu, G.; Luo, C.; Chang, X.; Duan, J.; Lin, Q.; Xu, B.; et al. Response of ecosystem respiration to warming and grazing during the growing seasons in the alpine meadow on the Tibetan plateau. *Agric. For. Meteorol.* **2011**, *151*, 792–802. [CrossRef]
57. Chen, H.; Zhu, Q.; Peng, C.; Wu, N.; Wang, Y.; Fang, X.; Gao, Y.; Zhu, D.; Yang, G.; Tian, J.; et al. The impacts of climate change and human activities on biogeochemical cycles on the Qinghai-Tibetan Plateau. *Glob. Change Biol.* **2013**, *19*, 2940–2955. [CrossRef]
58. Chen, N.; Zhu, J.; Zhang, Y.; Liu, Y.; Li, J.; Zu, J.; Huang, K. Nonlinear response of ecosystem respiration to multiple levels of temperature increases. *Ecol. Evol.* **2019**, *9*, 925–937. [CrossRef]
59. Monson, R.K.; Lipson, D.L.; Burns, S.P.; Turnipseed, A.A.; Delany, A.C.; Williams, M.W.; Schmidt, S.K. Winter forest soil respiration controlled by climate and microbial community composition. *Nature* **2006**, *439*, 711–714. [CrossRef]
60. Pan, L.; Xiao, X.; Yao, Y.; Pan, B.; Yin, C.; Meng, C.; Qin, Y.; Zhang, C. Site-specific apparent optimum air temperature for vegetation photosynthesis across the globe. *Sci. Data* **2024**, *11*, 758. [CrossRef]
61. Tang, R.; He, B.; Chen, H.W.; Chen, D.; Chen, Y.; Fu, Y.H.; Yuan, W.; Li, B.; Li, Z.; Guo, L.; et al. Increasing terrestrial ecosystem carbon release in response to autumn cooling and warming. *Nat. Clim. Change* **2022**, *12*, 380–385. [CrossRef]
62. Abdalla, K.; Schierling, L.; Sun, Y.; Schuchardt, M.A.; Jentsch, A.; Deola, T.; Wolff, P.; Kiese, R.; Lehndorff, E.; Pausch, J.; et al. Temperature sensitivity of soil respiration declines with climate warming in subalpine and alpine grassland soils. *Biogeochemistry* **2024**, *167*, 1453–1467. [CrossRef]
63. Aurela, M.; Tuovinen, J.-P.; Laurila, T. Carbon dioxide exchange in a subarctic peatland ecosystem in northern Europe measured by the eddy covariance technique. *J. Geophys. Res. Atmos.* **1998**, *103*, 11289–11301. [CrossRef]
64. Zhao, L.; Li, Y.; Xu, S.; Zhou, H.; Gu, S.; Yu, G.; Zhao, X. Diurnal, seasonal and annual variation in net ecosystem CO_2 exchange of an alpine shrubland on the Qinghai–Tibetan Plateau. *Glob. Change Biol.* **2006**, *12*, 1940–1953. [CrossRef]
65. Richardson, A.D.; Black, T.A.; Ciais, P.; Delbart, N.; Friedl, M.A.; Gobron, N.; Hollinger, D.Y.; Kutsch, W.L.; Longdoz, B.; Luyssaert, S.; et al. Influence of spring and autumn phenological transitions on forest ecosystem productivity. *Philos. Trans. R. Soc. B* **2010**, *365*, 3227–3246. [CrossRef]